



OPEN

Swarm shedding in networks of self-propelled agents

Jason Hindes¹✉, Victoria Edwards^{1,2}, Klimka Szwaykowska Kasraie³, George Stantchev¹ & Ira B. Schwartz¹

Understanding swarm pattern formation is of great interest because it occurs naturally in many physical and biological systems, and has artificial applications in robotics. In both natural and engineered swarms, agent communication is typically local and sparse. This is because, over a limited sensing or communication range, the number of interactions an agent has is much smaller than the total possible number. A central question for self-organizing swarms interacting through sparse networks is whether or not collective motion states can emerge where all agents have coherent and stable dynamics. In this work we introduce the phenomenon of swarm *shedding* in which weakly-connected agents are ejected from stable milling patterns in self-propelled swarming networks with finite-range interactions. We show that swarm shedding can be localized around a few agents, or delocalized, and entail a simultaneous ejection of all agents in a network. Despite the complexity of milling motion in complex networks, we successfully build mean-field theory that accurately predicts both milling state dynamics and shedding transitions. The latter are described in terms of saddle-node bifurcations that depend on the range of communication, the inter-agent interaction strength, and the network topology.

Much attention has been given to the study of multi-agent swarms that can self organize and form complex spatiotemporal patterns from very basic rules governing individual dynamics^{1–3}. Natural swarms typically involve the coupling of large numbers of mobile agents, and can be seen in many fascinating biological systems from flocks of birds^{4–6}, to schools of fish^{7,8}, crowds of people⁹, and colonies of bacteria and insects^{10,11}. Similar self-organization phenomena occur in self-propelled, active-matter systems^{12–16}. Both theoretical and applied research has focused on understanding the principles underlying collective motion^{1,2,17–24}, and how such principles can be instantiated in mobile-robotic systems^{25–29}. Applications for the latter range from mapping³⁰, to exploration²⁷, and resource allocation^{31–33}.

Agent interactions in both natural and decentralized robotic swarms are typically sparse and local due to finite bandwidth and communication range^{29,34,35}. Sparse and heterogeneous network effects on swarming are understood analytically, mostly within the context of controlling teams of mobile agents through decentralized, average consensus algorithms^{20,36–38}. Typically, such systems involve sharing speed and heading data directly among agents, and are somewhat limited in their dynamics, e.g., to flocking, where consensus forms around a network-wide velocity. On the other hand, physically inspired models, where collective motion emerges from the more basic interplay of position-dependent forces and self-propulsion energy, have typically assumed global, homogeneous, or lattice communication topology^{39–45}. For instance, early robotics experiments based on such nonlinear-physics models, also assumed all-to-all coupling^{42,46}—making them difficult to scale to larger systems and less controlled environments. Since the latter class of models derive from basic physical principles, they showcase a broader spectrum of emergent motion patterns, and can more easily incorporate, e.g., active-matter dynamics^{15,43} and collective motion on arbitrary surfaces⁴⁷. Recent work has begun to address network structure in such physically-inspired swarming systems, including how topology affects robustness to noise⁴⁸ and how heterogeneous topology drives the formation of hybrid motion states⁴⁹. Yet, much remains unknown about how complex topology influences the dynamical stability of swarms with general nonlinear interactions and under what circumstances a sparse swarming network can maintain coherent motion of all its agents—especially in the much broader range of collective-motion patterns without rigid velocity consensus.

To make progress, we consider a well known physics-based model of mobile agents moving under the influence of self-propulsion, damping, and pairwise interaction forces^{41,43,48,50}, to which we add explicit sparse networks that mediate and constrain the inter-agent interactions^{42,49}. In the absence of interactions, each swimmer will tend to a fixed speed, which balances its self-propulsion and damping but has no preferred direction⁴⁷. The agents are assumed to interact through a network, whose topology is *fixed in time*, and given by a *simple static*

¹U.S. Naval Research Laboratory, Washington, DC 20375, USA. ²University of Pennsylvania, Philadelphia, PA 19104, USA. ³Georgia Tech Research Institute, Atlanta, GA 30318, USA. ✉email: jason.hindes@nrl.navy.mil

graph with an adjacency matrix: $A_{ij} = 1$, if agents i and j are connected, and zero otherwise⁵¹. The matrix A_{ij} will be generated from a variety of standard graph models specified below. In addition to the topology, the interaction between two agents will be associated with a strength that is assumed to decay exponentially with their relative distance, namely $\exp\{-|\mathbf{r}_j - \mathbf{r}_i|/l_2\}$, where \mathbf{r}_i is the position-vector for the i th agent in three spatial dimensions (and similarly for agent j), and l_2 is a constant measuring the characteristic length scale for maintaining connections. The connection strength can be thought of as an edge weight in the corresponding (weighted) interaction graph model, which for example is commonly used as a simple approximation for ad-hoc wireless networks⁵². Altogether, the interaction graph matrix takes the form

$$W_{ij} = A_{ij} \exp\{-|\mathbf{r}_j - \mathbf{r}_i|/l_2\} \quad (1)$$

for agents i and j .

Given an interaction graph, we assume that there is a force between two agents, either a real physical force or a control force, that tends to minimize a scalar potential function of the agent positions. As in many other works, we assume that the interaction force is elastic (spring-like) and tends to maintain a characteristic separation between two agents, l_1 ^{41,43,48,50,53}. Combining all of the basic physics-ingredients gives a dynamic model for the i th agent

$$\ddot{\mathbf{r}}_i = [\alpha - \beta|\dot{\mathbf{r}}_i|^2]\dot{\mathbf{r}}_i + \lambda \sum_j A_{ij} e^{-\frac{|\mathbf{r}_j - \mathbf{r}_i|}{l_2}} \frac{\mathbf{r}_j - \mathbf{r}_i}{|\mathbf{r}_j - \mathbf{r}_i|} (|\mathbf{r}_j - \mathbf{r}_i| - l_1), \quad (2)$$

where α is a self-propulsion constant, β is a damping constant, and λ is a coupling constant^{39–41,50,54}; the symbol $\ddot{\mathbf{r}}_i$ denotes the acceleration of the i th agent, while $\dot{\mathbf{r}}_i$ denotes its velocity. Note that the aforementioned weighted interaction matrix, $W_{ij} = A_{ij} \exp\{-|\mathbf{r}_j - \mathbf{r}_i|/l_2\}$, that appears in the second term of Eq. (2) controls directly the dynamics of pairwise interactions among swarming agents, and in that sense it serves as a surrogate for an actual communication model. This simplification allows us to build intuition about the behavior of a swarming system with heterogeneous sparse connectivity while avoiding the complexity of modeling communication channel effects and wireless network implementations.

Our approach in the following is to study the stability of basic swarming patterns in the model Eq. (2), and in particular understand how pattern stability is lost in a given network, A_{ij} , as we change the communication range l_2 , and the strength of inter-agent coupling, λ . A successful theory in this regard should predict how strong the coupling must be, and how far the communication range, in order to stabilize collective motion states in given a network. Such a theory could also provide insights for guiding robotics experiments with autonomous ground, surface, and aerial vehicles^{42,53,46}, which have used Eqs. (2), and similar variants, as an underlying control law. In particular, these experiments were effectively all-to-all in terms of communication, and thus, our analysis can help scale-up similar experiments to larger robotic swarms in less controlled environments.

Methods

First, when simulating the model Eq. (2) with random initial positions and velocities we find two primary collective-motion patterns: flocking and milling⁵⁵. In the former, a swarm's center of mass translates at a steady, fixed velocity. Agents move on average with the center-of-mass velocity and undergo slow oscillations around a fixed relative formation that is a steady-state solution of the over-damped dynamics⁵⁶. In contrast, in the milling state (MS) agents rotate around a stationary center of mass with no macroscopic consensus in velocity. Whether or not a swarm converges to one of these two states (or possibly others), depends on initial conditions, swarm parameters, and network topology. In this work, we focus on the MS since it emerges from the broadest range of initial conditions, e.g., random initial headings for the agents. An example MS is shown in Fig. 1 given a Waxman random geometric graph of connections for the topology A_{ij} , where nodes are connected according to an exponential probability distribution in their initial separations⁵⁷. The network had a distribution of connections per node (or degree, k) that was somewhat heterogeneous, ranging from $k = 4$ to $k = 42$, with an average and standard deviation, $\langle k \rangle = 20$ and $\sigma = 7$, respectively; see supplementary material appendix for more network details. In terms of spatio-temporal initial conditions, throughout this work, we assign every agent a location selected uniformly at random inside a cube with unit side length, centered at the origin. Similarly, the velocities are assigned uniformly at random inside a velocity-cube with unit side length, centered at zero-velocity. Then, Eq. (2) is integrated to a time $t = 1000$, so that the resulting behavior is non-transient. We find that such conditions are sufficient to produce stable milling patterns.

Important features of the MS dynamics can be seen in both panels (a) and (b) of Fig. 1. In the first, a snapshot in time shows that agents are arranged at various instantaneous distances from the center of the swarm with a broad distribution of velocities (there is no easily discernible pattern in the heading arrows). Qualitatively, higher-degree agents wander near the center, while lower-degree agents wander at the periphery. In the second panel (b), we plot the normalized Fourier spectra for several example agents, where the peak frequency is set to unity. Though the Fourier spectra are non-trivial and broad in general, a basic pattern emerges when we note that the peaks follow the ordering of degree, from left to right: low to high degree nodes.

These observations can be made more precise by plotting the time-averaged distance to the swarm center of mass and the peak frequency versus the degree. Both are computed by integrating Eq. (2) over an additional $\Delta t = 200$ from the initial conditions specified in the first paragraph of 'Methods' section. Examples are shown in Fig. 2 for two network topologies (A_{ij}): a power-law degree distributed network and a Waxman graph. The power-law network was constructed using the configuration model and a fraction of nodes with degree k , $g(k) \sim k^{-2.58}$. The network was also heterogeneous with an average degree $\langle k \rangle = 20$ and a standard deviation $\sigma = 20$; further network details are given in the supplementary material. Simulation results are shown with

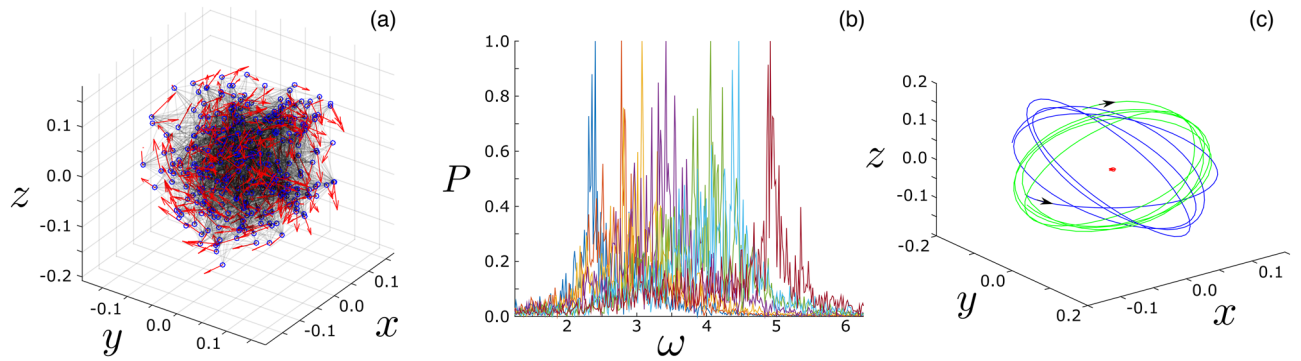


Figure 1. Milling state in self-propelled swarming networks. **(a)** Snap-shot of milling in which agents are drawn with blue circles, velocities with red arrows, and network edges with black-lines. **(b)** The Fourier spectra (normalized, absolute value) of seven randomly selected agents drawn with different colors. For reference, the leftmost spectrum corresponds to a $k = 8$ agent while the rightmost corresponds to $k = 40$. **(c)** Trajectory of a $k = 10$ agent (blue), $k = 20$ agent (green), and the swarm center of mass (red). The network topology was a Waxman geometric random graph with 300 agents and an average degree of 20. Other model parameters are: $\alpha = 1, \beta = 5, l_1 = 0.1, l_2 = 1,$ and $\lambda = 2$.

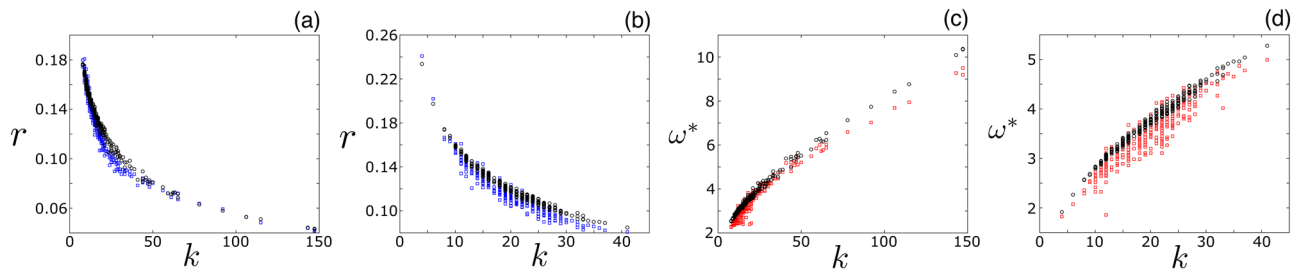


Figure 2. Averaged milling state oscillations. The average distance to the swarm’s center of mass versus the agent degree for a power-law network **(a)** and a Waxman geometric random graph **(b)**. Simulation results are shown with blue squares and mean-field predictions with black circles from solving Eqs. (3a–3b). Peak frequency from the Fourier spectra versus agent degree for the same power-law network **(c)** and Waxman geometric random graph **(d)**. Simulation results are shown with red squares and mean-field predictions with black circles. Each network was composed of 300 agents with an average degree of 20. Other model parameters are identical to Fig. 1.

blue and red squares. Despite the instantaneous complexity of the MS dynamics illustrated in Fig. 1, Fig. 2 suggests that the approximate behavior of every agent is to rotate on an orbit with some steady-state distance to the swarm’s center at a frequency that depends on its location in the network (and particular, on its topological degree k). To further illustrate the rotational dynamics, we show three example trajectories for a $k = 10$ agent (blue), a $k = 20$ agent (green), and the swarm center of mass (red) in Fig. 1c. The next step is to predict the center-of-mass distances r and frequencies ω , and understand their dependence on the model parameters and topology in quantitative detail.

Milling state mean field. We can approximate the behavior plotted in Fig. 2 by building a steady-state mean-field description of the MS. First, let us adopt spherical coordinates for convenience, e.g., for node i , $\mathbf{r}_i = r_i \cos \phi_i \sin \theta_i \hat{\mathbf{x}} + r_i \sin \phi_i \sin \theta_i \hat{\mathbf{y}} + r_i \cos \theta_i \hat{\mathbf{z}}$. Second, let us assume that every node travels on a circular orbit (approximately) with fixed radius and frequency, i.e., r_i and ω_i , respectively for node i . Third, let us orient our axes such that a test node i oscillates with $\theta_i = \omega_i t$ and $\phi_i = 0$. Fourth, let us substitute the ansatz, $\mathbf{r}_i = r_i \sin \omega_i t \hat{\mathbf{x}} + r_i \cos \omega_i t \hat{\mathbf{z}}$, for node i into Eq. (2). The result is three equations for each node that must be satisfied (one for each component of acceleration).

The final mean-field step is to approximate the interaction-sums in Eq. (2), by assuming that there is *no correlation* between the angles $\theta_i, \theta_j, \phi_i,$ and ϕ_j in the MS for any connected nodes i and j —the only correlation is in the radii by assumption. Therefore, from the perspective of node i , the angles for node j in the MS are equally-likely to take on any values during its orbit, and thus for every interaction-term in Eq. (2) we multiply by the probability that the angles are found within a small interval centered around θ_j and ϕ_j , $\sin \theta_j d\theta_j d\phi_j / 4\pi$ and integrate over θ_j and ϕ_j . Repeating the above for every node results in N root equations, e.g., $F_i(r_1, r_2, \dots, r_N) = 0$ for node i , where

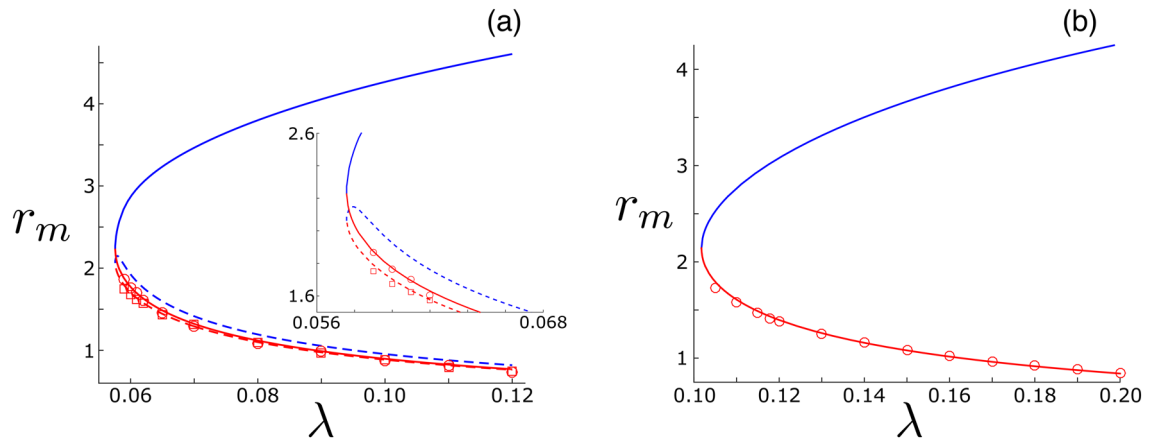


Figure 3. Distance from a swarm’s center versus coupling for agents with the lowest degree in their network. **(a)** Power-law network where simulation-determined values are plotted with red circles and squares for two agents that are directly connected and ejected at the first shedding transition. Mean-field predictions from solving Eqs. (3a–3b) are drawn for each node with solid and dashed lines: stable (red) and unstable (blue). The inset panel shows the same plot zoomed-in to the bifurcation. **(b)** Similar plot for a Waxman network topology, where only one agent is shed. Other model parameters are identical to Fig. 1.

$$F_i = \frac{\alpha}{\lambda\beta r_i} + \sum_j A_{ij} \int_0^\pi \frac{\sin \theta_j d\theta_j}{2} (r_j \cos \theta_j - r_i) e^{-d_{ij}/l_2} \left(1 - \frac{l_1}{d_{ij}}\right), \tag{3a}$$

$$d_{ij}(r_i, r_j, \theta_j) = \sqrt{r_j^2 + r_i^2 - 2r_i r_j \cos \theta_j}, \tag{3b}$$

and

$$\omega_i = \sqrt{\alpha/\beta}/r_i \tag{4}$$

The Eqs. (3a–3b) can be solved by numerically integrating the polar-angle θ -integrals and computing the r ’s through a quasi-Newton evaluation of Eqs. (3a). We note that in the limit of zero-repulsion, $l_1 \rightarrow 0$, each integral can be solved in closed-form and written as explicit functions of r_i and r_j . Numerical solutions of Eqs. (3a–3b) are plotted in Fig. 2 alongside simulation values and show good agreement, despite the very different network topologies used in each example, and thus demonstrating the robustness of our mean-field predictions to topological variation.

It is important to note that the behavior implied by Eq. (3a) is a mean-field approximation to the actual swarming dynamics in the MS. To get a better sense of this we return to Fig. 1c, which shows sample trajectories over a time interval of $\Delta t = 10$ for a $k = 10$ agent (blue), a $k = 20$ agent (green), and the swarm center of mass (red). For the first two agents, we can see that instead of rotating around a fixed plane, in fact, each agent wobbles and precesses over the course of several periods of its oscillation. However, as long as the precession occurs slowly relative to the dominant frequency (as they do in these examples) the mean-field approximation is fairly accurate. Another assumption of the mean field is that the swarm center of mass is stationary in time. In actuality, the center of mass fluctuates with a standard-deviation that is $O(1/N)$. Note that in Fig. 1c the red trajectory represents a small, finite-size vibration compared to the large amplitude oscillations of individual agents.

Notably, in the limit of long-range communication, $l_2 \gg 1$, and weak repulsive force between agents, $l_1 \ll 1$, solutions approach

$$r_i \approx \sqrt{\alpha/\beta\lambda k_i} \tag{5}$$

and $\omega_i \approx \sqrt{\lambda k_i}$, implying that the MS radii are expected to scale inversely with the square root of the coupling λ , and the degree of agents⁴². Note the degree of node i , $k_i = \sum_j A_{ij}$.

Results

In the MS a constant-magnitude centripetal force is supplied to every agent by the sum-total of its network interactions, which are weighted by the coupling constant, λ . The corresponding centripetal acceleration is constrained by the fact that the self-propulsion and damping forces must also balance, and hence the speed of every agent is $\sqrt{\alpha/\beta}$ within the mean-field approximation. Since, we are interested in the effect of reducing the coupling between agents in the network, consider what happens when λ is reduced, for example. As λ decreases, the average distance from the swarm’s center increases, according to Eq. (5), and agents are less tightly held by the interaction force. Two examples of this trend are shown in Fig. 3, where radii of the lowest-degree agents in two networks are plotted in red as function of λ . At some critical point λ_c , the lowest-degree agents approach

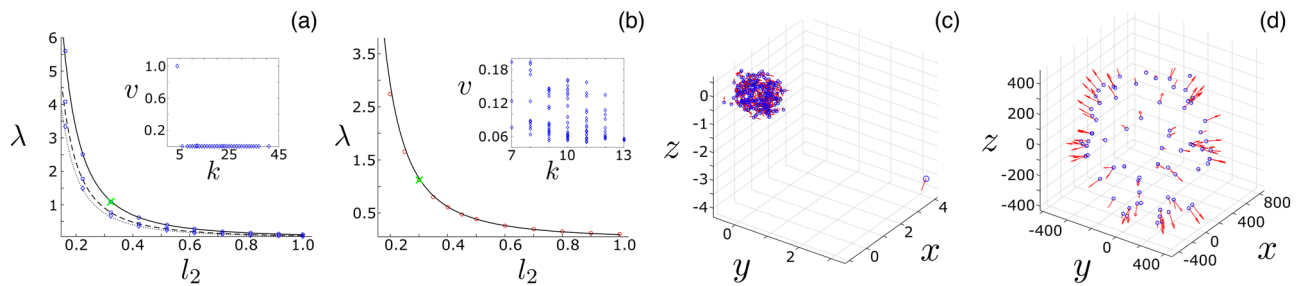


Figure 4. Shedding of agents from milling states. (a) Critical coupling for localized shedding in a Waxman geometric random graph. Points indicate simulation-determined values while lines indicate mean-field predictions. Plotted are the first three shedding transitions: $k = 4$ (circles, solid line), $k = 6$ (squares, dashed line), and $k = 8$ (diamonds, dotted line). (b) Critical coupling for the single, delocalized shedding transition in a Watts–Strogatz random graph. The Watts–Strogatz graph was composed of 100 agents with an average degree of 10. Inlet panels in (a) and (b) show the predicted unstable mode associated with the upper mean-field bifurcation by solving Eq. (6). Example snapshots for λ just below the respective transitions are shown in (c) and (d) for the two graphs. Locations for the snapshots within the diagrams (a) and (b) are specified with a green x. Other model parameters and plotting conventions are identical to Fig. 1.

the communication length scale, $r \sim l_2$, and it becomes stable for the network to simply eject such agents from the MS, and zero-out their interactions by letting them fly off to infinity: $W_{ij} \rightarrow 0$ for ejected node i . We call this transition in general, *swarm shedding*.

Qualitatively, if the low-degree agents are connected to higher-degree agents, as is typically the case in random degree-heterogeneous networks like the Waxman and power-law networks, shedding will only involve isolated lowest-degree agents. Both examples in Fig. 3 illustrate this pattern. In such networks, shedding occurs in a distinct sequence: first the lowest-degree agent is shed at some $\lambda_{c,1}$, then the second lowest at some $\lambda_{c,2} < \lambda_{c,1}$, etc. We denote these transitions as *localized shedding* from the MS, since instability is associated with one (or $\mathcal{O}(1)$) agents. On the other hand if the lowest-degree agents are connected to other low-degree agents, as in weakly connected homogenous networks where most agents have $k \sim \langle k \rangle \sim \mathcal{O}(1)$, then when a low degree agent is shed it will cause other agents to effectively go out of communication range and be shed, resulting in a cascade of low-degree agent shedding. Because instability involves $\mathcal{O}(N)$ agents at the critical point in this case, we call such transitions *delocalized shedding*.

Examples of each kind of shedding are shown in Fig. 4. On the left, a sequence of localized sheddings occurs in a swarm with a Waxman network topology. In subpanel (a) we plot the first three transitions as a function of the communication length scale. Simulation-determined transition points are drawn with blue markers, and correspond to the smallest $\lambda(l_2)$ for which a swarm, which is initially prepared in a MS, keeps all agents from reaching a distance $10 \cdot l_2$ from the center-of-mass after an integration time of $t = 1000$. In subpanel (a), the top series represents shedding of a $k = 4$ agent, the middle to $k = 6$, and the bottom to $k = 8$. In the panel (c), we show a snapshot of the swarm for λ just below the critical point. We can see that one agent flies away from the rest of the network (in the bottom right corner), and will continue on to infinity. In contrast, in panels (b) and (d) a single delocalized shedding transition occurs given a Watts-Strogatz network topology, where the underlying degree-distribution was sharply peaked around the average $\langle k \rangle = 10$ with a standard deviation $\sigma = 1.4$. For reference, the Watts-Strogatz model produces “small-world” networks by adding a small fraction of random short-cuts to a ring lattice⁵⁹. As shown in Fig. 4d, all agents fly away from the swarm center, independently, for λ just below the critical point. The swarm effectively breaks up into a collection of disconnected agents, with $W_{ij} \rightarrow 0$ for all but a small fraction of interactions with $A_{ij} \neq 0$. See supplementary material for more network details, including degree-distribution plots.

Shedding theory. Using our mean-field theory it is possible to predict the shedding transition in Fig. 4, and thus gain a more quantitative understanding. Within the mean-field, shedding corresponds to the disappearance of stable solutions to Eq. (3a) in *saddle-node* bifurcations (SNs), shown in Fig. 3 where two branches of MS radii collide—the red and blue curves. Consequently, we expect a single eigenvalue of the linearized Eq. (3a) to approach zero as $\lambda \rightarrow \lambda_c$. We can find a general condition to determine the critical coupling at the SN through the following. First, we compute the derivatives of Eqs. (3a) with respect to the MS radii, $\partial F_m / \partial r_m$, which constitute the elements of a Jacobian matrix, \underline{J} , where $J_{mn} \equiv \partial F_m / \partial r_n$. Then, we impose that the the largest eigenvalue of \underline{J} , denoted μ_N , is zero:

$$\mu_N = 0, \quad (6)$$

where $\mu_1 \leq \mu_2 \leq \dots \leq \mu_N$ are the eigenvalues of \underline{J} . When Eq. (6) is added to Eqs. (3a), the result is $N + 1$ equations for the first shedding transition point, $\lambda_{c,1}$, and the associated MS radii.

Numerical mean-field solutions for shedding transitions in Fig. 4 are plotted with lines and show excellent agreement with simulations over a range of communication length scales, l_2 . Shedding-transition simulations were performed by first integrating Eq. (2) from the initial conditions specified in the first paragraph of ‘Methods’ section for fixed parameters, starting at $\lambda = 6$. Then, λ was reduced by 0.001 and the system was integrated for another $\Delta t = 1000$. At which point, the number of agents within a distance $10 \cdot l_2$ from the center of mass was

recorded, λ reduced again, and the process repeated. Measured transition values corresponded to λ at which the number of agents within the $10 \cdot l_2$ range changed from one increment to another. This set of numerical experiments was repeated for multiple values of l_2 .

In addition, the predicted unstable mode at the SN associated with the eigenvalue $\mu_N = 0$, i.e., $\mathbf{0} \equiv J \mathbf{v}_N$, is plotted in the inlets of (a) and (b) for both examples; in particular for each agent i , $v_{N,i}$ is plotted versus its degree k_i . We can see that the non-zero components of the mode predict accurately which agents are shed in Fig. 4c, d. In the localized case, the mode in the inlet of (a) is approximately zero for all agents, except one at $k = 4$. In contrast, for the delocalized case the mode in the inlet of (b) is homogeneously distributed across all agents. We note that for predicting the second and third localized transition curves in panel (a), we simply remove nodes from the network with non-zero elements in this mode. In fact, for the all three curves in Fig. 4a, there is only one such node for each transition line. Each subsequent (lower) mean-field transition line is computed from Eq. (3a) using the *residual network*, and deleting edges in A_{ij} that correspond to ejected nodes in the previous shedding transition.

An interesting consequence of our SN theory is the prediction that shedding still occurs even in the limit of zero-repulsion, $l_1 \rightarrow 0$, which one can check by looking for solutions in such cases. The implication is that shedding depends on the finite communication range, l_2 , and the sparse network topology, $\langle k \rangle \ll N$. We can demonstrate this by performing an explicit calculation for random networks that are approximately degree-homogeneous, where all nodes are assumed to have the same degree, $k_i \approx \langle k \rangle \forall i$, as in the Watts–Strogatz example. For such networks, we expect the MS radii to be equal, $r_i = r \forall i$. Consequently, the integral in Eq. (3a) can be simply evaluated. By usefully defining a normalized radius, $a \equiv r/l_2$, Eq. (3a) reduces to

$$0 = \frac{\alpha}{\beta \langle k \rangle l_2^2 \lambda} + \frac{4a^3 + 6a^2 + 6a + 3 - 3e^{2a}}{2a^2 e^{2a}}. \quad (7)$$

We can calculate the critical threshold, λ_c , by setting the derivate of the right-hand-side of Eq. (7) with respect to a equal to zero, as implied by Eq. (6). The result is a root equation for the critical (normalized) radius a_c . The radius is independent of all other model parameters and satisfies

$$0 = 4a_c^4 + 4a_c^3 + 6a_c^2 + 6a_c + 3 - 3e^{2a_c}. \quad (8)$$

It is easy to check that Eq. (8) has a single positive solution, $a_c = 1.41872271133$ —quantitatively demonstrating that shedding occurs when MS radii reach the l_2 communication length scale, $a \approx 1$. Finally, by combining Eqs. (7–8), the critical coupling reduces nicely to the product of model parameters and a pure number

$$\lambda_c = \frac{\alpha}{\beta \langle k \rangle l_2^2} \frac{2a_c^2 e^{2a_c}}{3e^{2a_c} - 4a_c^3 - 6a_c^2 - 6a_c - 3}. \quad (9)$$

For reference, the pure number in Eq. (9) is 4.240937302. For the Watts–Strogatz network the prediction Eq. (9) is nearly indistinguishable from the more accurate calculation that employs the exact network Jacobian, Eq. (6). In fact, the two predictions agree to within 1% for all l_2 when $l_1 = 0$.

On the other hand, in degree-heterogeneous swarming networks, such as the power-law and Waxman networks, single-node shedding is the most typical, and the general SN condition Eq. (6) reduces to

$$\lambda_c = \alpha / \beta r_m^2 \sum_j A_{mj} \int_0^\pi \frac{\sin \theta_j d\theta_j}{2} \frac{e^{-\frac{d_{mj}}{l_2}} (r_j \cos \theta_j - r_m)^2}{d_{mj}} \left(\frac{l_1 - d_{mj}}{(r_j \cos \theta_j - r_m)^2} - \frac{l_1}{d_{mj}^2} + \frac{(1 - l_1/d_{mj})}{l_2} \right), \quad (10)$$

where the subscript m corresponds to the node with the minimum degree, $k_m = \min_i \{k_i\}$. If multiple agents have degree k_m , and are not directly connected in the network, then Eq. (10) is only satisfied for one node—the node with the largest radius. Predictions in Fig. 4a were computed from Eq. (10) in this way.

A related localized shedding case occurs in heterogeneous networks when two (or more generally, n) nodes with degree k_m are directly connected. In this case, all n nodes are shed simultaneously, and it is straightforward to generalize Eq. (10). The calculation reduces to setting the determinant of an n -by- n Jacobian sub-matrix to zero. For example in the power-law swarming network, the first shedding transition corresponds to the loss of two directly connected $k = 10$ agents in the MS. The radii of both nodes associated with this transition are plotted in Fig. 3a.

Discussion

In this work, we provided analytical insights into swarm cohesion under sparse interaction network constraints by adding explicit interaction graphs into a well known and general physics model for swarm pattern formation^{39–41,50,54}. Using the more general networked interactions, we introduced the phenomenon of swarm shedding whereby weakly-held agents in a swarming network are ejected from collective milling states, where there is no velocity consensus and no net motion of the swarm's center of mass. We distinguished between localized and delocalized shedding in degree-heterogeneous and homogeneous networks, respectively. In the former, one (or a small number) of agents are ejected from a mill as the coupling-strength or interaction range is reduced. In the latter, all nodes are ejected simultaneously as a swarm breaks up into effectively disconnected agents. Such transitions were accurately described in terms of saddle-node bifurcations of circular-orbit limit cycles within a mean-field approximation, and agreed well with numerical simulations. This network-based swarming theory will guide new physics-inspired swarm robotics experiments, where earlier instantiations

effectively assumed all-to-all communication, and hence, may not be easily scalable to larger robotic swarms, especially in complex environments^{42,46}.

Though our analysis dealt directly with self-propelled swarming networks with position-dependent, finite-range interactions, our basic approach could easily be extended to a broader range of models. An important next step would be to extend our analysis to network systems with explicit time-dependent topology, and not just position-dependent interaction weights—particularly for swarming applications in robotics. Another important extension would be to consider noise-induced shedding, since our theory implies the existence of saddle milling states through which networks are expected to break-up into smaller swarms in the presence of noise⁶⁰. Finally, understanding the differences between shedding from milling states and shedding from flocking states in swarming networks, represents an interesting question for future comparisons. These and other implications of our shedding theory will be explored in future autonomous mobile-robot experiments.

Together, this work takes an important step toward further understanding the role of complex network topology in facilitating coherent motion in self-organized swarms of mobile agents, and provides insight into how such patterns can change stability through the loss of agents.

Received: 2 February 2021; Accepted: 17 May 2021

Published online: 29 June 2021

References

- Vicsek, T. & Zafeiris, A. Collective motion. *Phys. Rep.* **517**, 71. <https://doi.org/10.1016/j.physrep.2012.03.004> (2012).
- Marchetti, M. C. *et al.* Hydrodynamics of soft active matter. *Rev. Mod. Phys.* **85**, 1143. <https://doi.org/10.1103/RevModPhys.85.1143> (2013).
- Aldana, M., Dossetti, V., Huepe, C., Kenkre, V. M. & Larralde, H. Phase transitions in systems of self-propelled agents and related network models. *Phys. Rev. Lett.* **98**, 095702. <https://doi.org/10.1103/PhysRevLett.98.095702> (2007).
- Young, G. F., Scardovi, L., Cavagna, A., Giardina, I. & Leonard, N. E. Starling flock networks manage uncertainty in consensus at low cost. *PLoS Comput. Biol.* **9**, 1–7. <https://doi.org/10.1371/journal.pcbi.1002894> (2013).
- Ballerini, M. *et al.* Interaction ruling animal collective behavior depends on topological rather than metric distance: evidence from a field study. *Proc. Natl. Acad. Sci.* **105**, 1232–1237. <https://doi.org/10.1073/pnas.0711437105> (2008).
- Cavagna, A. *et al.* Flocking and turning: a new model for self-organized collective motion. *J. Stat. Phys.* **158**, 601–627. <https://doi.org/10.1007/s10955-014-1119-3> (2015).
- Tunström, K. *et al.* Collective states, multistability and transitional behavior in schooling fish. *PLoS Comput. Biol.* **9**, 1–11. <https://doi.org/10.1371/journal.pcbi.1002915> (2013).
- Calovi, D. S. *et al.* Swarming, schooling, milling: phase diagram of a data-driven fish school model. *New J. Phys.* **16**, 015026. <https://doi.org/10.1088/1367-2630/16/1/015026> (2014).
- Rio, K. & Warren, W. H. The visual coupling between neighbors in real and virtual crowds. *Transp. Res. Proc.* **2**, 132–140 (2014). <https://doi.org/10.1016/j.trpro.2014.09.017>. The Conference on Pedestrian and Evacuation Dynamics. (PED 2014), 22–24 October 2014 (Delft, The Netherlands, 2014).
- Polezhaev, A., Pashkov, R., Lobanov, A. I. & Petrov, I. B. Spatial patterns formed by chemotactic bacteria *Escherichia coli*. *Int. J. Dev. Biol.* **50**, 309. <https://doi.org/10.1387/ijdb.052048ap> (2006).
- Li, J. & Sayed, A. H. Modeling bee swarming behavior through diffusion adaptation with asymmetric information sharing. *EURASIP J. Adv. Signal Process.* **2012**, 18. <https://doi.org/10.1186/1687-6180-2012-18> (2012).
- Bär, M., Großmann, R., Heidenreich, S. & Peruani, F. Self-propelled rods: insights and perspectives for active matter. *Annu. Rev. Condens. Matter Phys.* **11**, 441–466. <https://doi.org/10.1146/annurev-conmatphys-031119-050611> (2020).
- Doostmohammadi, A., Ignés-Mullol, J., Yeomans, J. M. & Sagués, F. Active nematics. *Nat. Commun.* **9**, 3246. <https://doi.org/10.1038/s41467-018-05666-8> (2018).
- Solon, A. *et al.* Pressure is not a state function for generic active fluids. *Nat. Phys.* **11**, 673. <https://doi.org/10.1038/nphys3377> (2015).
- Fodor, E. *et al.* How far from equilibrium is active matter?. *Phys. Rev. Lett.* **117**, 038103. <https://doi.org/10.1103/PhysRevLett.117.038103> (2016).
- Cichos, F., Gustavsson, K., Mehlig, B. & Volpe, G. Machine learning for active matter. *Nat. Mach. Intell.* **2**, 94–103. <https://doi.org/10.1038/s42256-020-0146-9> (2020).
- Woodhouse, F. G., Ronellenfötsch, H. & Dunkel, J. Autonomous actuation of zero modes in mechanical networks far from equilibrium. *Phys. Rev. Lett.* **121**, <https://doi.org/10.1103/PhysRevLett.121.178001> (2018).
- Woillez, E., Zhao, Y., Kafri, Y., Lecomte, V. & Tailleur, J. Activated escape of a self-propelled particle from a metastable state. *Phys. Rev. Lett.* **122**, 258001. <https://doi.org/10.1103/PhysRevLett.122.258001> (2019).
- Desai, J. P., Ostrowski, J. P. & Kumar, V. Modeling and control of formations of nonholonomic mobile robots. *IEEE Trans. Robot. Autom.* **17**(6), 905–908. <https://doi.org/10.1109/70.976023> (2001).
- Jadbabaie, A., Jie Lin & Morse, A. S. Coordination of groups of mobile autonomous agents using nearest neighbor rules. *IEEE Trans. Autom. Control* **48**, 988–1001 (2003). <https://doi.org/10.1109/TAC.2003.812781>.
- Tanner, H. G., Jadbabaie, A. & Pappas, G. J. Stable flocking of mobile agents part ii: dynamic topology. In *42nd IEEE International Conference on Decision and Control (IEEE Cat. No.03CH37475)*, vol. 2, 2016–2021 Vol.2 (2003). <https://doi.org/10.1109/CDC.2003.1272911>.
- Tanner, H. G., Jadbabaie, A. & Pappas, G. J. Stable flocking of mobile agents, part i: fixed topology. In *42nd IEEE International Conference on Decision and Control (IEEE Cat. No.03CH37475)*, vol. 2, 2010–2015 Vol.2 (2003). <https://doi.org/10.1109/CDC.2003.1272910>.
- Gazi, V. Swarm aggregations using artificial potentials and sliding-mode control. *IEEE Trans. Robot.* **21**, 1208–1214. <https://doi.org/10.1109/TRO.2005.853487> (2005).
- Tanner, H. G., Jadbabaie, A. & Pappas, G. J. Flocking in fixed and switching networks. *IEEE Trans. Autom. Control* **52**, 863–868. <https://doi.org/10.1109/TAC.2007.895948> (2007).
- Aguilar, J. *et al.* A review on locomotion robophysics: the study of movement at the intersection of robotics, soft matter and dynamical systems. *Rep. Prog. Phys.* **79**, 110001. <https://doi.org/10.1088/0034-4885/79/11/110001> (2016).
- Siegwart, R., Nourbakhsh, I. & Scaramuzza, D. *Autonomous Mobile Robots* (MIT Press, London, 2011).
- Miller, I. D. *et al.* Mine tunnel exploration using multiple quadrupedal robots. *IEEE Robot. Autom. Lett.* **5**, 2840–2847. <https://doi.org/10.1109/LRA.2020.2972872> (2020).
- Pickem, D. *et al.* The robotarium: A remotely accessible swarm robotics research testbed. In *2017 IEEE International Conference on Robotics and Automation (ICRA)*, 1699–1706 (2017). <https://doi.org/10.1109/ICRA.2017.7989200>.

29. Kagan, E., Shvalb, N. & Ben-Gal, I. *Autonomous Mobile Robots and Multi-Robot Systems: Motion-Planning, Communication, and Swarming* (Wiley, 2020).
30. Ramachandran, R. K., Elamvazhuthi, K. & Berman, S. *An Optimal Control Approach to Mapping GPS-Denied Environments Using a Stochastic Robotic Swarm*, 477–493 (Springer International Publishing, Cham, 2018).
31. Li, H. *et al.* Decentralized stochastic control of robotic swarm density: Theory, simulation, and experiment. In *2017 IEEE/RSJ International Conference on Intelligent Robots and Systems (IROS)*, 4341–4347 (2017). <https://doi.org/10.1109/IROS.2017.8206299>.
32. Berman, S., Halasz, A., Kumar, V. & Pratt, S. Bio-inspired group behaviors for the deployment of a swarm of robots to multiple destinations. In *Proceedings 2007 IEEE International Conference on Robotics and Automation*, 2318–2323 (2007). <https://doi.org/10.1109/ROBOT.2007.363665>.
33. Hsieh, M. A., Halász, A., Berman, S. & Kumar, V. Biologically inspired redistribution of a swarm of robots among multiple sites. *Swarm Intell.* **2**, 121–141. <https://doi.org/10.1007/s11721-008-0019-z> (2008).
34. Rosenthal, S. B., Twomey, C. R., Hartnett, A. T., Wu, H. S. & Couzin, I. D. Revealing the hidden networks of interaction in mobile animal groups allows prediction of complex behavioral contagion. *Proc. Natl. Acad. Sci.* **112**, 4690–4695. <https://doi.org/10.1073/pnas.1420068112> (2015).
35. Mesbahi, M. & Egerstedt, M. *Graph Theoretic Methods in Multiagent Networks* (Princeton University Press, Princeton, NJ, 2010).
36. Cucker, F. & Smale, S. Emergent behavior in flocks. *IEEE Trans. Autom. Control* **52**, 852–862. <https://doi.org/10.1109/TAC.2007.895842> (2007).
37. Ferrante, E. *et al.* A self-adaptive communication strategy for flocking in stationary and non-stationary environments. *Nat. Comput.* **13**, 225–245. <https://doi.org/10.1007/s11047-013-9390-9> (2014).
38. Mateo, D., Kuan, Y. K. & Bouffanais, R. Effect of correlations in swarms on collective response. *Sci. Rep.* **7**, 10388. <https://doi.org/10.1038/s41598-017-09830-w> (2017).
39. Levine, H., Rappel, W. J. & Cohen, I. Full velocity difference model for a car-following theory. *Phys. Rev. E* **63**, 017101. <https://doi.org/10.1103/PhysRevE.63> (2000).
40. D’Orsogna, M. R., Chuang, Y. L., Bertozzi, A. L. & Chayes, L. S. Surface reactivity and quantum-size effects on the electronic density decay length of ultrathin metal films. *Phys. Rev. Lett.* **96**, <https://doi.org/10.1103/PhysRevLett.96> (2006).
41. Mier-y-Teran-Romero, L., Forgoon, E. & Schwartz, I. B. Coherent pattern prediction in swarms of delay-coupled agents. *IEEE Trans. Robot.* **28**, 1034–1044. <https://doi.org/10.1109/TRO.2012.2198511> (2012).
42. Szwajkowska, K. *et al.* Collective motion patterns of swarms with delay coupling: Theory and experiment. *Phys. Rev. E* **93**, 032307. <https://doi.org/10.1103/PhysRevE.93> (2016).
43. Ferrante, E., Turgut, A. E., Dorigo, M. & Huepe, C. Collective motion dynamics of active solids and active crystals. *New J. Phys.* **15**, 095011. <https://doi.org/10.1088/1367-2630/15/9/095011> (2013).
44. Albi, G., Balagué, D., Carrillo, J. A. & von Brecht, J. Stability analysis of flock and mill rings for 2nd order models in swarming. *SIAM J. Appl. Math.* **74**, 794. <https://doi.org/10.1137/13091779X> (2014).
45. Bernoff, A. & Topaz, C. A primer of swarm equilibria. *SIAM J. Appl. Dyn. Syst.* **10**, 212. <https://doi.org/10.1137/100804504> (2011).
46. Edwards, V. *et al.* Delay induced swarm pattern bifurcations in mixed reality experiments. *Chaos* **30**, 073126. <https://doi.org/10.1063/1.5142849> (2020).
47. Hindes, J., Edwards, V., Kamimoto, S., Stantchev, G. & Schwartz, I. B. Stability of milling patterns in self-propelled swarms on surfaces. *Phys. Rev. E* **102**, 022212. <https://doi.org/10.1103/PhysRevE.102> (2020).
48. Turgut, A. E., Boz, I. C., Okay, I. E., Ferrante, E. & Huepe, C. Interaction network effects on position- and velocity-based models of collective motion. *J. R. Soc. Interface* **17**, 20200165. <https://doi.org/10.1098/rsif.2020.0165> (2020).
49. Hindes, J., Szwajkowska, K. & Schwartz, I. B. Hybrid dynamics in delay-coupled swarms with “motherhood” networks. *Phys. Rev. E* **94**, 032306. <https://doi.org/10.1103/PhysRevE.94> (2016).
50. Erdmann, U., Ebeling, W. & Mikhailov, A. S. Dynamic network modeling of two-phase drainage in porous media. *Phys. Rev. E* **71**, 051904. <https://doi.org/10.1103/PhysRevE.71> (2005).
51. Newman, M. *Networks: An Introduction* (Oxford University Press Inc, USA, 2010).
52. Dettmann, C. P., Georgiou, O. & Pratt, P. Spatial networks with wireless applications. *Comptes Rendus Physique* **19**, 187–204. <https://doi.org/10.1016/j.crhy.2018.10.001> (2018).
53. Hindes, J., Edwards, V., Kamimoto, S., Triandaf, I. & Schwartz, I. B. Unstable modes and bistability in delay-coupled swarms. *Phys. Rev. E* **101**, 042202. <https://doi.org/10.1103/PhysRevE.101> (2020).
54. Minguzzi, E. Rayleigh’s dissipation function at work. *Eur. J. Phys.* **36**, 035014. <https://doi.org/10.1088/0143-0807/36/3/035014> (2015).
55. Chuang, Y.-li, D’Orsogna, M. R., Marthaler, D., Bertozzi, A. L. & Chayes, L. S. State transitions and the continuum limit for a 2d interacting, self-propelled particle system. *Physica D: Nonlinear Phenomena* **232**, 33–47. <https://doi.org/10.1016/j.physd.2007.05.007> (2007).
56. Carrillo, J., Huang, Y. & Martin, S. Nonlinear stability of flock solutions in second-order swarming models. *Nonlinear Anal. Real World Appl.* **17**, 332–343. <https://doi.org/10.1016/j.nonrwa.2013.12.008> (2014).
57. Waxman, B. M. Routing of multipoint connections. *IEEE J. Select. Areas Commun.* **6**, 1617–1622. <https://doi.org/10.1109/49.12889> (1988).
58. Newman, M. E. J., Strogatz, S. H. & Watts, D. J. Random graphs with arbitrary degree distributions and their applications. *Phys. Rev. E* **64**, 026118. <https://doi.org/10.1103/PhysRevE.64> (2001).
59. Watts, D. J. & Strogatz, S. H. Collective dynamics of ‘small-world’ networks. *Nature* **393**, 440–442. <https://doi.org/10.1038/30918> (1998).
60. Hindes, J. & Schwartz, I. B. Large order fluctuations, switching, and control in complex networks. *Sci. Rep.* **7**, 10663. <https://doi.org/10.1038/s41598-017-08828-8> (2017).

Acknowledgements

JH and IBS were supported by the U.S. Naval Research Laboratory funding (N0001419WX00055), the Office of Naval Research (N0001419WX01166) and (N0001419WX01322), and the Naval Innovative Science and Engineering award. VE was supported through the U.S. Naval Research Laboratory Karles Fellowship. GS was supported through the Office of Naval Research funding (N0001420WX01237).

Author contributions

J.H., I.B.S, K.S, and G.S conceived the problem. J.H, V.E, and I.B.S performed the analysis. J.H, V.E, I.B.S, and G.S. wrote the main manuscript. All authors reviewed the manuscript.

Competing interests

The authors declare no competing interests.

Additional information

Supplementary Information The online version contains supplementary material available at <https://doi.org/10.1038/s41598-021-92748-1>.

Correspondence and requests for materials should be addressed to J.H.

Reprints and permissions information is available at www.nature.com/reprints.

Publisher's note Springer Nature remains neutral with regard to jurisdictional claims in published maps and institutional affiliations.



Open Access This article is licensed under a Creative Commons Attribution 4.0 International License, which permits use, sharing, adaptation, distribution and reproduction in any medium or format, as long as you give appropriate credit to the original author(s) and the source, provide a link to the Creative Commons licence, and indicate if changes were made. The images or other third party material in this article are included in the article's Creative Commons licence, unless indicated otherwise in a credit line to the material. If material is not included in the article's Creative Commons licence and your intended use is not permitted by statutory regulation or exceeds the permitted use, you will need to obtain permission directly from the copyright holder. To view a copy of this licence, visit <http://creativecommons.org/licenses/by/4.0/>.

This is a U.S. Government work and not under copyright protection in the US; foreign copyright protection may apply 2021